JACS
JOURNAL OF THE AMERICAN CHEMICAL SOCIETY
Article
pubs.acs.org/JACS

Y_3MnAu_5: Three Distinctive *d*-Metal Functions in an Intergrown Cluster Phase

Saroj L. Samal,[†,‡] Abhishek Pandey,[†,§] David C. Johnston,[†,§] and John D. Corbett*[,†,‡]

[†]Ames Laboratory-USDOE, [‡]Department, of Chemistry, and [§]Department of Physics and Astronomy, Iowa State University, Ames, Iowa 50011, United States

Supporting Information

ABSTRACT: The new Y_3MnAu_5 intermetallic phase is obtained from the arc-melted elements in virtually quantitative yields after annealing at 1000 °C for ~3 d. Its remarkable structure [rhombohedral, $R\bar{3}$, Z = 6; a = 8.489(1) Å, c = 18.144(2) Å] consists of a 2:1 cubic-close-packed intergrowth between edge-shared Mn-centered Au rhombohedra (Mn@Au_8) with gold-centered antiprismatic (Au@Y_6) clusters via a common gold network. Magnetic susceptibility (χ) data for Y_3MnAu_5 were fitted by a Curie–Weiss law. The Curie constant indicates a large effective moment corresponding to nearly localized Mn spins S = 5/2, and the Weiss temperature demonstrates the dominance of ferromagnetic (FM) interactions. An antiferromagnetic (AFM) transition at T_N = 75 K and a possible spin reorientation transition at 65 K were observed. Analysis of the χ data for $T < T_N$ suggests a planar noncollinear helical AFM structure that arises from competing AFM interactions between FM-aligned layers of spins in the *ab*-plane with a turn angle of 69° between the spins along the helix *c*-axis. A magnetic field-induced spin flop transition is observed below T_N. Spin-polarized LMTO-LSDA calculations indicate an ~2 eV splitting of the Mn 3d states and a metallic ground state, and their COHP analyses demonstrate that ~81% of the total Hamilton populations originate from heteroatomic polar Y–Au and Mn–Au bonding. The Mn 3d, Y 4d, and Au 5d characteristics are remarkably diverse: localized and magnetically polarized for Mn; reducing and cationic for Y; and relativistically strongly bonded and oxidizing for Au, bonding of the latter two being broadly delocalized.

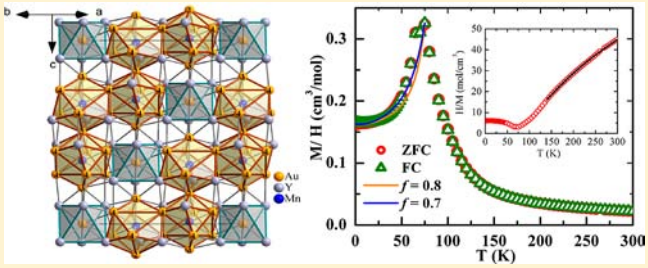

INTRODUCTION

Exploratory syntheses in new intermetallic systems have always been of prime importance in the discovery of novel ternary (or higher order) phases, especially because such materials are largely unclassified, quite unpredictable, and lack simple bonding or valence rules.[1,2] Very diverse polar intermetallic phases are generally obtained from reactions between an electropositive alkali (A) or alkaline-earth (Ae) metal, a relatively electronegative late transition metal, and a main group *p* metal or metalloid. Among the sixth-period transition metals, gold has recently been found to be especially effective in affording new and unusual cluster, network or tunnel constructions with a range of cations, evidently because of substantial relativistic effects[3] that enhance gold's bonding to later metals, for example, in many A/Ae–Au–Tr systems (Tr (triel) = Ga, In, Tl).[4−13] Decreases in total valence electron count (VEC) through inclusion of Zn or Cd in place of Tr yield new structural chemistry,[14,15] some of which appear to depend on critical size (packing) effects as well. For example, the Na–Au–Cd system contains a novel condensed cluster network $Na_6Cd_{16}Au_7$ built of segregated tetrahedral stars of Cd networked with individual Au atoms,[14] whereas a change to Zn leads to a pair of new Na–Au–Zn tunnel structures only with Na.[15] Switches of the electropositive component to a more tightly bound *Ae* or a rare-earth (*R*) metal generally produce substantial changes, particularly to higher symmetry, more uniform and stronger bonding. Thus, the ternary $BaAu_xZn_{13-x}$ system ($0 < x < 8$) consists of a broad substitutional derivative of cubic $BaZn_{13}$, as well as a closely related tetragonal phase.[16] Numerous ternary examples of related intermetallic rare-earth-metal phases have also been reported.[17−19]

Continuing our efforts to explore new intermetallic chemistry, we have now introduced the 3d element Mn as the third component in several active metal–Mn–Au systems. In these instances, the more weakly bonding alkali metals Na to Cs do not form any ternary phases. This was the prime reason for the present inclusion of the rare-earth elements Y, Gd, etc., as active metals. The choice of Mn as the 3d member was based in part on the extensive literature on magnetic properties of binary Y–Mn systems,[20−24] the likelihood that a magnetic ground state would occur in any ternary product, and the expectation that Au would have substantial effects on the bonding and properties of these. No ternary R–Au–Mn example has been reported. Several new Ca–Au–Mn phases are also presently under study.

Received: November 8, 2012
Published: December 21, 2012

   dx.doi.org/10.1021/ja3110208 | *J. Am. Chem. Soc.* 2013, 135, 910–917

EXPERIMENTAL SECTION

Syntheses. All the reactants and products were handled inside a glovebox filled with dry N_2 (≤0.1 ppm H_2O by volume). New products were explored in ternary phases of Y, La, Nd, Gd, Dy, or Tm (99.995%, Ames Laboratory) with Mn (99.99%, Micron Metals) and Au (99.99%, BASF). The weighed reactants were sealed inside Ta tubing containers that were subsequently sealed in an evacuated silica jacket. The contents were allowed to react at 1000 °C for 24 h, quenched, and equilibrated at 800 °C for 4 days. Longer reaction times gave the same results. The Y−Au−Mn system evidently contains only one ternary compound and that in the gold-rich region, Y_3MnAu_5. Reactions in yttrium-richer regions led to the familiar Y_2Au and Y_3Au_2, and in the Mn-richer part, to binary Y−Mn phases. Single crystals of Y_3MnAu_5 were first grown from a YMn_2Au_2 composition and later, X-ray pure polycrystalline samples (Supporting Information, Figure S1) were synthesized (according to the structurally refined composition) by arc-melting stoichiometric amounts of Y, Au and premade $MnAu_3$. It must be noted that arc-melting of stoichiometric amounts of Y, Au, and Mn always results in mixtures of Y_3MnAu_5 and YAu_2 because of loss of Mn through volatilization. For crystal growth, the as-cast sample was annealed at 1000 °C for 3−4 d and then quenched in ice water. The compound has metallic luster, and the powder is visibly stable in air at room temperature for at least a few days. Lattice dimensional data for the isostructural phases R_3MnAu_5, R = Gd, Dy, and Tm, are listed in Table S1, Supporting Information. Reactions with R = La or Nd did not yield this product, which is not unusual.[25]

X-ray Diffraction Studies. X-ray diffraction measurements on the polycrystalline samples were performed at room temperature with the aid of a Stoe Stadi P powder diffractometer equipped with an image plate and Cu Kα_1 radiation (λ = 1.54059 Å). The ground samples were dispersed between two acetate films in the glovebox with the aid of a small amount of grease and then enclosed in the airtight STOE sample holder. The lattice parameter refinements and the profile fitting of powder X-ray data employed the General Structure Analysis System (GSAS) software.[26]

Single crystal X-ray diffraction measurements were performed at room temperature with the aid of a Bruker SMART CCD diffractometer equipped with Mo Kα radiation (λ = 0.71073 Å). The data were collected over a 2θ range of ∼3° to ∼56° as three sets of 606 frames with 0.3° scans in ω and 20 s/frame exposures. The reported compound showed a trigonal R-centered lattice, and the intensity statistics indicated a centrosymmetric space group. The reflection intensities were integrated with the SAINT program in the SMART software package.[27] Empirical absorption corrections were made with the aid of the SADABS program.[28] The space group $R\bar{3}$ was determined with the help of XPREP and SHELXTL 6.1.[29] The structure was solved by direct methods and subsequently refined on $|F^2|$ with combinations of least-squares refinements and difference Fourier maps.

Direct methods yielded six independent atomic positions, and the assignments of four as Au1−Au4 and two as Y and Mn according to their separations all turned out to be correct. The Au1 and Au2 atoms on $\bar{3}$ sites have only six and eight neighbors, respectively, and naturally refine with larger isotropic displacement parameters, about twice the size of those for Au3 and Au4 in sites with higher multiplicities and more neighbors, ∼0.022 versus 0.013 Å^2, respectively. Neither atom mixings nor partial occupancies gave suitable alternate explanations. The converged refinements with anisotropic displacement ellipsoids gave R_1 = 0.0310 and R_W = 0.0556 and maximum residuals of 2.6 and −3.1 e/Å^3 that were 1.2 and 0.72 Å from Au4, respectively, probably because of limitations in the absorption corrections for Au. Some crystallographic and refinement parameters for the compound are given in Table 1. The atomic positions and important bond distances are listed in Tables 2 and 3, and the anisotropic displacement parameters appear in Supporting Information as Table S2. The cif file is also provided in Supporting Information.

Electronic Structure Calculations. Self-consistent electronic structure calculations were performed by means of tight binding linear-muffin-tin-orbital (TB-LMTO) methods within the atomic sphere approximation (ASA).[30] Exchange and correlation were treated in the local spin density approximation (LSDA). Furthermore, the simplest model that would allow the observed antiferromagnetic coupling was employed, that in S.G. R3 with two independent Mn atoms. The radii of the WIGNER-SEITZ spheres were assigned automatically so that the overlapping potentials would be the best possible approximations to the full potential.[31] Their radii were Y = 2.02 Å, Mn = 1.60 Å, Au1 = 1.50 Å, Au2 = 1.73 Å, Au3 = 1.49 Å, and Au4 = 1.37 Å. No additional empty spheres were needed subject to 18% overlap restriction between atom-centered spheres. Basis sets of Y 5s, 4d, (5p); Au 6s, 6p, 5d, (4f); and Mn 4s, 4p, 3d (downfolded orbitals in parentheses) were employed, and the reciprocal space integrations were performed by means of the tetrahedron method. Scalar relativistic corrections were included. The calculations were carried out at 12 × 12 × 12 k points in the irreducible wedge of the Brillouin zone. For bonding analysis, the energy contributions of all filled electronic states for selected atom pairs were calculated by the crystal orbital Hamilton population (COHP method).[32] These were given a weighted integration up to the Fermi energy (E_F) to provide ICOHP data, total Hamilton populations (Table 3 and Supporting Information Table S3), which are approximations of relative bond populations. The COHP analyses provide the contributions of the covalent parts of particular pairwise interactions to the total bonding energy of the crystal.

Table 1. Some Crystal Data and Structural Refinement Parameters for Y_3MnAu_5

compound	Y_3MnAu_5
formula weight	1306.5 g/mol
space group, Z	$R\bar{3}$ (No.148), 6
unit cell parameters (Å)	a = 8.489(1) Å, c = 18.144(2) Å
V cell (Å^3)	1132.3(4) Å^3
d_{calcd} (g cm^{-3})	11.49
θ range for data collection	2.99−28.18°.
index range	$-11 \le h \le 10$, $-10 \le k \le 11$, $-24 \le l \le 23$
reflns collected	3226
independent obs. reflect.	604 (R_{int} = 0.0457)
data/params	604/30
R/R_w ($I > 2\sigma$)[a]	0.0310/0.0556
R/R_w (all data)	0.0352/0.0589
largest diff. peak, hole (e Å^{-3})	2.59 [1.21 Å from Au4]
	−3.13 [0.72 Å from Au4]

[a] $R = \Sigma||F_o| - |F_c||/\Sigma|F_o|$; $R_w = [\Sigma w(|F_o| - |F_c|)^2/\Sigma w(F_o)^2]^{1/2}$; $w = 1/\sigma_F^2$.

Physical Property Measurements. Magnetic field (H) and temperature (T) dependent magnetization (M) measurements were carried out using a superconducting quantum interference device (SQUID) magnetometer (Quantum Design, Inc.). The diamagnetic contributions of the transparent gel caps used for sample holders were measured separately and applied to the data. Specific heat (C_p) measurements were performed by the relaxation method in H = 0 in a Quantum Design physical properties measurement system (PPMS). The ac transport option of the PPMS was used to measure the four-probe resistivities (ρ) of the polycrystalline material. The $\rho(T)$ was measured at two different applied magnetic fields, 0 and 5 T (see Supporting Information).

RESULTS AND DISCUSSION

Crystal Structure. The compound Y_3MnAu_5, isolated from gold-rich regions of the Y−Mn−Au system, crystallizes in a new rhombohedral structure type, space group $R\bar{3}$, Z = 6, a = 8.489(1) Å, c = 18.144(2) Å (trigonal setting), as illustrated in Figure 1. Isostructural phases were also obtained for Gd, Dy, and Tm analogues according to X-ray powder diffraction data, Supporting Information Table S1. This remarkable structure is in effect a 2:1 intergrowth of the two quite different Mn−Au

dx.doi.org/10.1021/ja3110208 | J. Am. Chem. Soc. 2013, 135, 910−917

Table 2. Y_3MnAu_5. Atom Coordinates and Wyckoff Positions in Space Group $R\bar{3}$, and Isotropic Equivalent Displacement Parameters (U_{iso})

atom	Wyckoff	symm.	x	y	z	U_{iso}
Y	18*f*	1	0.2799(2)	0.9901(2)	0.0990(1)	0.0127(3)
Mn	6*c*	3	0	0	0.3451(2)	0.0137(1)
Au1	3*a*	−3	0	0	0	0.0242(3)
Au2	3*b*	−3	0	0	1/2	0.0201(3)
Au3	6*c*	3	0	0	0.1972(1)	0.0128(2)
Au4	18*f*	1	0.6203(1)	0.0053(1)	0.0633(1)	0.0129(2)

Table 3. Bond Length Ranges in and Average Molar ICOHP Values for Y_3MnAu_5 from Spin Polarized Calculations[a]

bond	length (Å)	−ICOHP/bond (ave.)	n^b	−ICOHP (eV)/cell	percentage (%)
Y−Y	3.622(2)−3.875(2)	0.267	27	7.21	2.6
Y−Mn	3.391(2)−3.706(2)	0.42	36	15.48	5.5
Y−Au	2.899(1)−3.239(2)	0.97	162	157.1	56.0
Mn−Au	2.682(2)−2.945(2)	1.40	48	67.20	23.9
Au−Au	2.925(1)−3.578(1)	0.487	69	33.60	12.0

[a]Intercluster d(Mn−Mn) ≥ 4.92(1) Å. [b]number of bonds per cell.

and Y−Au substructures by means of a common gold network or sheath. These are illustrated both separately and combined as [110] sections in Figure 1. Part a shows the 6-fold distribution of a single type of Mn atoms (blue), each of which is encased in a distorted rhombohedron (bicapped trigonal antiprism) of eight gold atoms. Some further details of the Mn environments will be relevant to magnetic data to follow. The clusters are bonded into dimers along *c* through shared Au2 vertices on $\bar{3}$ sites [Figure 1a], which means that each cluster is polar with only 3-fold rotational symmetry. (The other end of each cluster is capped by a terminal Au3 atom which leaves room for the neighboring Au1@Y_6 clusters along *c*.) Each Mn atom also has two bands of $(Au4)_3$ atoms in general positions around the cluster waist. The sharing of pairs of these Au4 waist atoms with three like (inverted) polyhedra (Figure 2) generates the open layers of clusters normal to *c* and parallel to the *a*−*b* plane, Figure 1a. In detail, the Mn atoms are displaced from the seemingly common planes at z = 1/3, 2/3, [Figure 1a] by

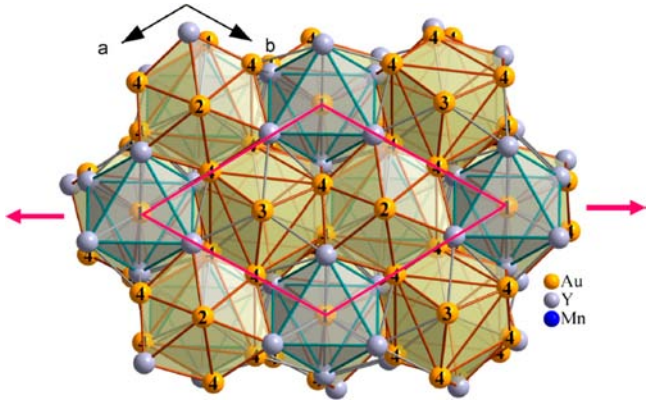

Figure 2. (001) projection of the unit cell of Y_3MnAu_5 (outlined in magenta) with the entire Au@Y_6 cluster columns around Au1 atoms at the origin included (blue). The four nearest neighbor Mn@Au_8 clusters at the top and bottom (yellow) complete the three-layer sequence of adjoining (110) sections along (1$\bar{1}$0) (the short diagonal of the basal face). Note the $(Au4)_6$ antiprisms around the waists of yellow Mn@Au_8 clusters that surround the (hidden) Mn atoms and bridge between the clusters. (The magenta arrows mark the plane of the [110] section.).

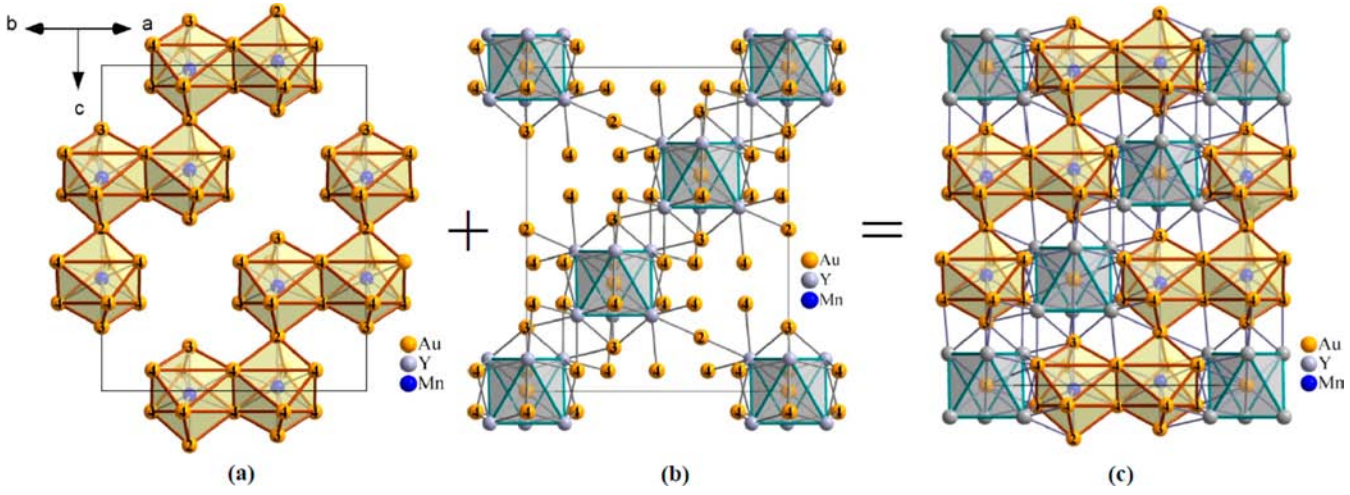

Figure 1. (110) view of the structure of Y_3MnAu_5. (a) The Mn atoms center distorted rhombohedra (bicapped trigonal antiprisms) of eight gold atoms. Each also shares pairs of Au4 waist atoms with three like polyhedra to generate open layers parallel to the *a*−*b* plane that are further interconnected along *c* via Au2 atoms. (b) Au1 atoms center trigonal antiprisms of Y (Au1@Y_6) that are interconnected via the common gold network in (a). (c) The condensed $(Mn@Au_8)_2$ and Au@Y_6 polyhedra that define the rhombohedral structure (trigonal basis), a cubic-close-packed array of condensed clusters that is slightly compressed along *c*.

dx.doi.org/10.1021/ja3110208 | J. Am. Chem. Soc. 2013, 135, 910−917

±0.214 Å, following the displacement of the more pyramidal Au2 cap at the inversion point.

The countervailing one-third of the structure is a remarkable and most unexpected variation; three identical Y_6 antiprisms per cell (gray, $\bar{3}$ symmetry), each centered by an otherwise isolated Au1 atom at (0,0,0), (1/3,2/3,2/3), and (2/3,1/3,1/3) [Figure 1b]. The direct Y−Y interactions within each antiprism, 4.19−4.33 Å, are relatively small because of the size of the centering Au1. The gold network atoms shown in Figure 1a are also bonded externally to one or more Y_6 units at vertices, edges, and faces, but these geometric details about the Y_6 groups are harder to describe compared with those in the Mn-centered array in Figure 1a. (The 32 Au neighbors around each Y_6 antiprism are illustrated and categorized in Figure S2, Supporting Information.)

The result of superposition of parts a and b to give Figure 1c can be easily recognized as the trigonal representation of the rhombohedral structure that is generated by the intergrowth of two ($Mn@Au_8$) and one ($Au@Y_6$) substructures in a cubic-close-packed manner with horizontal sequences ...ABC... [The c axis is compressed about 15% from the ideal cubic parent: ($\sqrt{6}a$ = 20.79 Å), c_o = 18.144 Å.] The somewhat taller $Au@Y_6$ antiprisms relative to the $Mn@Au_6$ antiprisms are evident in the [110] section, as well as the appreciable Au3−Y bonding marked here by gray lines between the Au3 caps in the $Mn@Au_8$ units and the adjoining Y_6 antiprisms. (Figure 1b shows the totality of Au−Y bonding.) Distances within the whole structure (listed earlier in Table 3 and Supporting Information Table S3) are generally reasonable considering the delocalized bonding and the complex functionalities, with ranges of ∼0.25−0.50 Å within examples of each bond type.

Other aspects of the [110] section of the structure can also be seen in the wider [001] cross section (the projection along c) in Figure 2 in which the unit cell projection and its longer diagonal are marked in magenta. The cubic close packing order of the layers is also explicit along that diagonal. The (001) view shown also includes the four neighboring $Mn@Au_8$ groups to illuminate the broader view. These also clarify (1) the important role of the Au4 dimers that circumscribe each $Mn@Au_8$ cluster and are shared between $Mn@Au_8$ rhombohedra in the a−b plane [Figure 1a], (2) that the $Mn@Au_8$ portions are somewhat larger in cross section than the Y_6 units, and (3) that some adaptation of the bridging between the two cluster types is noticeable in their relative rotations. A side view of Figure 2 in perspective appears in Supporting Information Figure S3. This is along the short diagonal of the trigonal projection ($1\bar{1}0$) and gives an in-depth view of the three independent layers normal to the (110) section in Figure 1c.

In foresight, the polar Y−Au interactions are dominant both in number and in their total crystal orbital Hamilton populations (ICOHP, ∼bond orders), whereas the collective Mn−Au contacts around each Mn are fewer in number but greater in population per contact. The phase is 55 at.% Au, but the remaining Au−Au interactions are less bonding, in effect because the structure utilizes most of the Au atoms in stronger heteropolar bonds elsewhere. Also, the Y−Y and Y−Mn distances are relatively large in this arrangement and their effects on bonding, smaller, whereas the Mn atoms are well separated within the gold network and their direct Mn−Mn interactions, negligible. These aspects of bonding will be pursued further after the magnetic studies are described.

Magnetic Measurements. The temperature dependences of the molar magnetic susceptibilities $\chi \equiv M/H$ of polycrystalline Y_3MnAu_5 under various conditions are shown in Figures 3 and 4. The sharp cusp in the $\chi(T)$ data in Figure 3 at 75 K

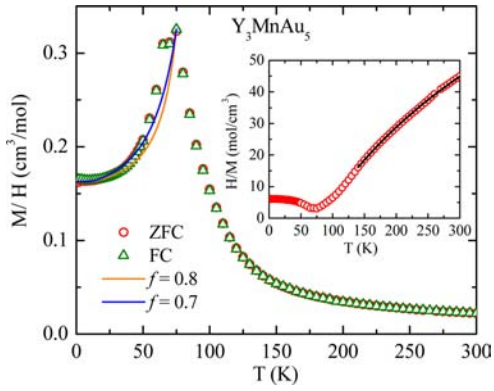

Figure 3. Zero-field-cooled (ZFC) and field-cooled (FC) magnetic susceptibility $\chi \equiv M/H$ of Y_3MnAu_5 versus temperature T measured at H = 0.1 T, where M is the magnetization and H is the applied magnetic field. The solid curves are fits using the expression described in the text and Supporting Information. Inset: ZFC $\chi^{-1}(T)$ data and a fit by eq 1.

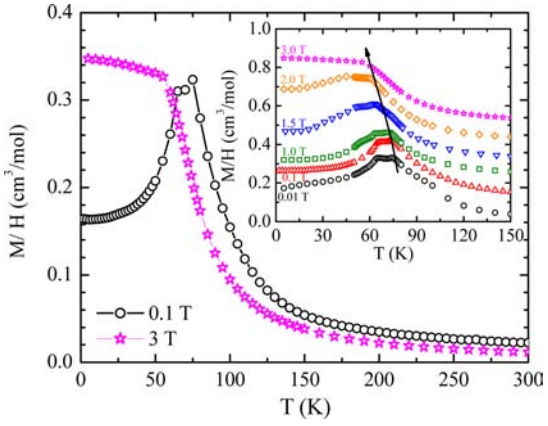

Figure 4. Magnetic susceptibility $\chi \equiv M/H$ versus temperature T of Y_3MnAu_5 at two different fields H = 0.1 and 3 T. The inset shows $\chi(T)$ between 5 and 150 K at six different fields. For clarity, the data in the inset taken at increasing fields have been successively shifted upward by 0.1 cm^3/mol.

indicates the occurrence of long-range antiferromagnetic (AFM) ordering at that temperature, which is designated as the Néel temperature (T_N). The zero-field-cooled (ZFC) and field-cooled (FC) measurements overlap each other, indicating that the data are free from blocking or pinning effects, further supporting the occurrence of long-range AFM ordering at T_N. Assuming that the magnetism in Y_3MnAu_5 originates from local magnetic moments on the Mn atoms, we fitted the $\chi(T)$ data between 140 and 300 K by the modified Curie−Weiss law

$$\chi(T) = \chi_0 + \frac{C}{T - \theta_p} \quad (1)$$

where χ_0 is the temperature-independent contribution to χ, C is the Curie constant, and θ_p is the Weiss temperature.

The resultant fit is satisfactory (inset, Figure 3) with the fitted values of the parameters being χ_0 = 0.0065(8) cm^3/mol, C = 3.5(2) cm^3 K/mol, and θ_p = 76(4) K. The value of C yields

dx.doi.org/10.1021/ja3110208 | J. Am. Chem. Soc. 2013, 135, 910−917

an effective magnetic moment $\mu_{eff} = (8C)^{1/2} = 5.3(2)\ \mu_B$/f.u. for spectroscopic splitting factor $g = 2$, which is similar to the value $\mu_{eff} = g\,(S(S+1))^{1/2}\,\mu_B = 5.92\ \mu_B$ expected for a high-spin $S = 5/2$ state of Mn, again assuming $g = 2$. The large value of μ_{eff} and the satisfactory fit of the high-T $\chi(T)$ data by the modified Curie–Weiss law support the hypothesis that local (or quasi-local) magnetic moments can be associated with the Mn atoms in this system.

The value of $\chi(T = 0)/\chi\ (T_N)$ expected for a polycrystalline local-moment system exhibiting collinear AFM ordering is 2/3,[33] but for Y_3MnAu_5 we instead obtain the value 0.51(3) from Figure 3. This result suggests that the AFM order in Y_3MnAu_5 is noncollinear in nature, that is, where the ordered moments in the AFM state are not all aligned along the same axis. Another important feature of the $\chi(T)$ data is the large positive (ferromagnetic-like, FM) value $\theta_p = 76(4)$ K of the Weiss temperature, which indicates the presence of strong and dominant FM interactions between the Mn magnetic moments in addition to the AFM interactions required to cause the AFM transition. Also, in view of the likely noncollinear AFM structure of Y_3MnAu_5, competing (frustrating) interactions for AFM order are also required in a local moment model. Such competing AFM interactions are plausible considering the complexity of the bonding within the Mn network in Figures 1 and 2 (later). Below we develop a model of the AFM structure in which FM interactions occur between the Mn moments within the somewhat puckered layers of Mn atoms parallel to the trigonal a–b plane, and competing AFM interactions occur between nearest- and next-nearest Mn layers along the c-axis, respectively. The latter two competing interlayer AFM interactions can give rise to an AFM helix structure with a wave vector along the c-axis, in which all moments within a given a–b plane layer are ferromagnetically aligned with a given direction within the plane, but the direction of the FM-aligned moments rotate from layer to layer along the c-axis by an angle determined by the ratio of these two interactions.

The presence of dominant FM interactions in a material exhibiting AFM long-range order occurs in so-called A-type collinear AFMs, in which the ordered magnetic moments within a defined structural layer are aligned ferromagnetically (at an angle of 0° to each other), but the moments in adjacent layers are aligned antiferromagnetically (at an angle of 180° to each other). In those collinear AFMs, the polycrystalline average χ_P of the susceptibility is $\chi_P(T = 0)/\chi_P(T_N) = 2/3$ as noted above.[33] In Y_3MnAu_5, we instead observe $\chi_P(T = 0)/\chi_P(T_N) = 0.51(3)$ from Figure 3, so it is likely that Y_3MnAu_5 has an AFM structure different from collinear A-type ordering.[34]

To support our model for the magnetism of Y_3MnAu_5, we first discuss the Mn sublattice of the structure. The Mn atoms form open, slightly puckered trigonal a–b plane layers as shown in Supporting Information Figure S5. The shortest Mn–Mn distances are 4.92(1) Å in the layers and 5.621(2) Å between layers. These distances are much larger than typical Mn–Mn bonds, and the Mn spins must therefore interact through an indirect RKKY-type exchange interaction via the conduction electrons.[35] In view of these considerations, we propose that the dominant FM interactions are between Mn atoms within the same a–b plane. Below T_N, these FM interactions align the in-plane Mn moments ferromagnetically with respect to each other, but AFM interactions between the layers along the c-axis cause the overall magnetic structure to be AFM as in A-type AFMs. However, since $\chi_P(T = 0)/\chi_P(T_N) = 0.51(3)$ instead of 2/3, we propose that in contrast to A-type AFMs, the angle between the moments in successive planes is not 180° but rather a smaller, possibly incommensurate, value. We thus propose that the AFM structure is a planar helix in which the ordered moments are ferromagnetically aligned within each a–b plane of Mn atoms and the axis of the helix is the c-axis, as illustrated in Supporting Information Figure S6.

We now use our recent Weiss molecular field theory (MFT) predictions[34] for $\chi(T < T_N)$ of planar noncollinear helical AFM systems to test this model. In this MFT, the angle between the moments in adjacent layers depends on the ratio $\chi(T = 0)/\chi\ (T_N)$ and is calculated to be $kd = 69(2)°$ in Y_3MnAu_5 using the observed value $\chi(T = 0)/\chi\ (T_N) = 0.51(3)$ (see the Supporting Information). The fact that kd is in the range $0 < kd < 90°$ is consistent with our observation that the dominant interactions between the Mn spins are FM. Furthermore, good fits of our T-dependent $\chi(T \leq T_N)$ data for Y_3MnAu_5 by the MFT expression[34] for a helical AFM are obtained with the same magnetic moment turn angle of 69° between adjacent layers and for $f = \theta_p/T_N$ values of either 0.7 or 0.8 as shown in Figure 3. An investigation of the low-temperature magnetic structure of Y_3MnAu_5 using neutron diffraction measurements could test our model.

In addition to the AFM transition obvious from the presence of a sharp cusp at 75 K, the $\chi(T)$ data for Y_3MnAu_5 at $H = 0.1$ T exhibit a shallow minimum below 75 K followed by another weaker cusp at ~65 K (Figures 3 and 4). To probe this behavior further we carried out additional $M(T)/H$ measurements at closely spaced T intervals between 5 and 150 K at various values of H as shown in the inset of Figure 4. These data reveal three important features: (i) the above kink in $M(T)/H$ near 65 K in the low field measurements is reproduced, is most likely caused by a slight spin reorientation at this temperature, diminishes in height with increasing field and is absent at $H = 3$ T; (ii) the value of $T_N(H = 0) = 75$ K decreases with increasing H to a value of ~60 K at $H = 3$ T (see Supporting Information Figure S5); and (iii) at high fields the magnetization saturates below $T \approx 60$ K to a nearly constant value.

We also carried out isothermal $M(H)$ measurements as shown in Figure 5, where a field-induced spin-flop transition is observed, as follows. The M versus H data at fixed T are nearly proportional above T_N as expected in the paramagnetic regime. However, the isothermal measurements at 50 and 60 K show that M is nearly proportional to H below 1 T, but for $H > 1$ T

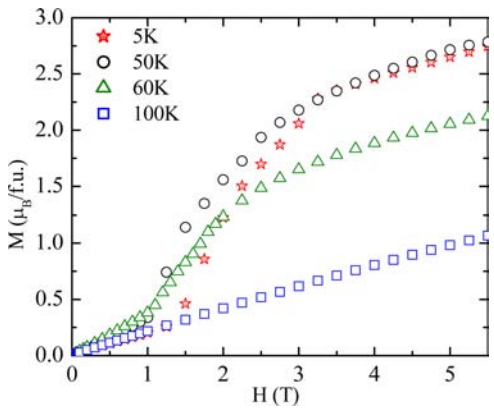

Figure 5. Isothermal magnetization M versus magnetic field H of Y_3MnAu_5 at the four temperatures indicated.

dx.doi.org/10.1021/ja3110208 | J. Am. Chem. Soc. 2013, 135, 910–917

M increases rapidly with increasing H before becoming approximately linear at higher H. From Figure 5, the value of M at $T = 5$ K $\ll T_N$ and at the maximum $H = 5.5$ T is 2.78 μ_B/f.u., which is only ~56% of the saturation value $\mu_{sat} = gS\mu_B = 5$ μ_B/Mn expected for the high-spin state ($S = 5/2$) of Mn with $g = 2$. From the large positive high-field slope in Figure 5, we infer that the saturation field is significantly higher than our high-field limit of 5.5 T. Thus we deduce that the S-shaped $M(H)$ behaviors in Figure 5 for $T < T_N$ arise from a spin-flop transition with an onset at $H \leq 1.5$ T in which the moments that are initially roughly parallel to the field flop toward a perpendicular orientation. A spin flop transition occurs when the magnetocrystalline anisotropy is sufficiently weak that the transition can be observed within the field range of the measurement. If the anisotropy field were zero, a spin flop transition would immediately occur upon applying even a small H. The spin flop transition field is expected to increase with decreasing T below T_N, which is confirmed by comparison of the data at $T = 60$ K with those at 5 K in Figure 5.

Heat Capacity Measurements. The $C_p(T)$ data for polycrystalline Y_3MnAu_5 are shown in Figure 6. The two

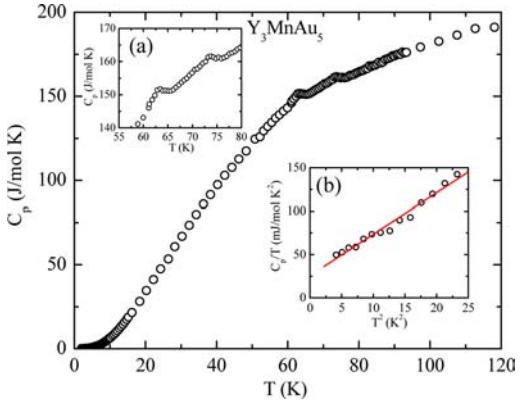

Figure 6. Heat capacity C_p versus temperature T for Y_3MnAu_5. Inset a: Expanded plot of the data near the two magnetic transitions. Inset b: C_p/T versus T^2 below 5 K. The straight line is a fit by eq 2 to the data between 2 and 5 K.

cusps in the data at 73 and 63 K, shown on an expanded scale in inset (a), correspond well with the AFM ordering transition at $T_N = 75$ K and the probable spin-reorientation transition at 65 K, respectively. The sawtooth-shaped cusps in $C_p(T)$ data suggest that the magnetic transitions are thermodynamically of second order. A conventional C_p/T versus T^2 plot at low temperatures is shown in inset b of Figure 6. These data were fitted by[35]

$$\frac{C_p}{T} = \gamma + \beta T^2 \tag{2}$$

where γ is the Sommerfeld coefficient of the electronic heat capacity and β is the coefficient of the low-T Debye T^3 lattice heat capacity. The fit is shown as the straight line in inset (b) of Figure 6 where the fitted values are $\gamma = 30(7)$ mJ/mol K^2 and $\beta = 4.2(8)$ mJ/mol K^4. We estimate the electronic density of states (DOS) at the Fermi energy E_F for both spin directions, $D(E_F)$, using[35]

$$\gamma = \frac{\pi^2 k_B^2}{3} D(E_F)(1 + \lambda_{e\text{-}ph}) \tag{3}$$

where $\lambda_{e\text{-}ph}$ is electron−phonon coupling constant which we set to zero as a first approximation. The experimental value of γ, eq 3 gives $D(E_F) = 13(3)$ states/eV f.u. for both spin directions. This value is a factor of 2 larger than the value of 6.6 states/eV f.u. obtained from the electronic structure calculations below. The origin of this factor of 2 discrepancy is evidently an electron−phonon coupling constant with a value $\lambda_{e\text{-}ph} \approx 1$. This $\lambda_{e\text{-}ph}$ value is sufficiently large that one would expect superconductivity to occur in Y_3MnAu_5 within our measurement T range via the electron−phonon interaction had the long-range AFM order not preempted it. We calculated a Debye temperature (Θ_D) of 162(11) K with[35]

$$\Theta_D = \left(\frac{12\pi^4 N_A k_B n}{5\beta}\right)^{1/3} \tag{4}$$

where N_A is Avogadro's number, k_B is Boltzmann's constant, and n is the number of atoms per f.u. ($n = 9$ for Y_3MnAu_5). This relatively small value of Θ_D likely results mainly from the large atomic weight of gold.

Electrical Resistivity Measurements. Figure 7 shows ρ versus T at $H = 0$ for a polycrystalline sample of Y_3MnAu_5. The

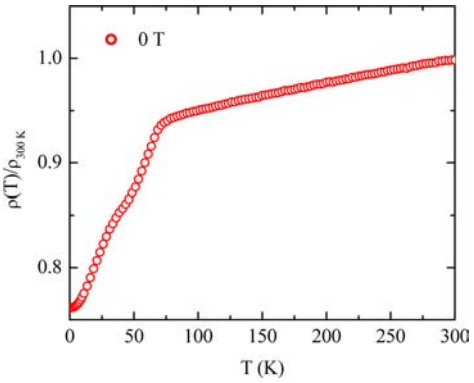

Figure 7. Electrical resistivity ρ for Y_3MnAu_5 versus temperature T, normalized by ρ(300 K).

ρ increases monotonically with increasing T, suggesting metallic character. This observation is consistent with the $C_p(T)$ measurements above and the electronic structure calculations below in which a significant DOS exists at E_F, which is characteristic of a metallic state. The $\rho(T)/\rho(300\text{ K})$ data also show a strong decrease with decreasing T below $T_N = 75$ K. This change most likely originates from the suppression of spin-disorder scattering below T_N. The $\rho(T)/\rho(300\text{ K})$ data also show a broad feature with an onset at ~60 K with decreasing T that might be related to the spin reorientation transition postulated above to occur near that T. The behavior of $\rho(T)$ at $H > 0$ is included in the Supporting Information, Figure S8.

Electronic Structure and Bonding. The electronic structure characteristics of Y_3MnAu_5 are particularly intriguing. The total DOS, individual atom and orbital projections from spin-polarized LMTO calculations in the local spin-polarized (LSDA) approximation for Y_3MnAu_5 (calculated for an AFM model in $R3$) are shown in Figure 8 in five parts: (a) the DOS for each element for both spin directions and the total; (b−d) orbital projections for Au, Mn, and Y, respectively; and (e) COHP data for each pairwise interaction per bond.mol. The sizable total DOS value at E_F, 6.6 states/eV f.u. for both spin

dx.doi.org/10.1021/ja3110208 | J. Am. Chem. Soc. 2013, 135, 910−917

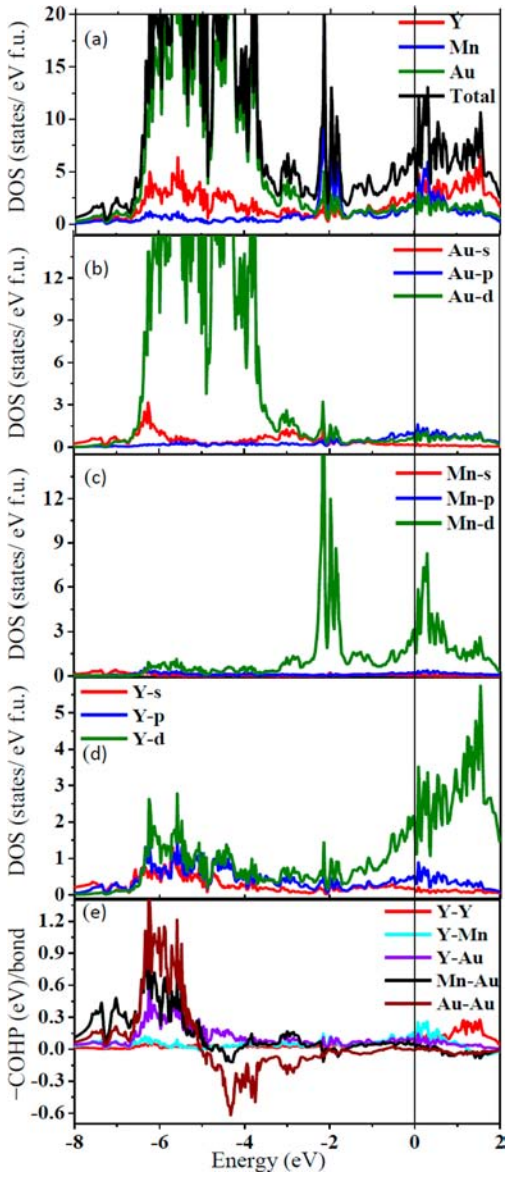

Figure 8. Spin-polarized LMTO-ASA calculations for Y_3MnAu_5 per f.u. (a) Densities-of-states (DOS) for different atom types for both spin directions. Partial projections of orbital components, per cell: (b) Au; (c) Mn 4s, 4p, 3d spin-polarized (both spins shown); (d) Y; (e) COHP values (eV per bond) for Y−Y (red), Y−Mn (blue), Y−Au (lavender), Mn−Au (black), and Au−Au (red-brown).

directions, indicates a metallic character. In detail, the *d* states of all three metals contribute to the orbital partial densities of states at E_F and to the COHP data, yet with distinctly different characteristics, namely, (b), the Au 5d orbital distributions over a broad band between approximately −7 to −2 eV are clearly the major sources of gold bonding within the polar framework, as better quantified by the COHP results (see e); (c) the relatively sharp pDOS peaks for Mn 3d orbitals at about −2.2 and +0.3 eV and their parallel contributions to bonding according to the COHP data (e) reflect strong spin polarization for only Mn, consistent with the large effective moment observed for it [μ_{eff} = 5.3(2) μ_B/f.u., above], and substantial Mn−Au (and some Mn−Y) bonding; (d), the Y 4d states are widely dispersed, those between −6 and −4 eV associated with Y−Au bonding, plus the few around −2.0 eV associated with Mn−Y bonding. As is common with rare-earth metal−Au−M compounds,[36,37] a substantial fraction of the Y 4d states are displaced to near and above E_F. These well reflect the role that the electropositive Y "cation" plays when paired with the strongly oxidizing gold component in 47% of all of the enumerated bond types in the structure (below).

Several interesting chemical bonding features of Y_3MnAu_5 can be deduced from the "crystal orbital" (COHP) plots [Figure 8e] and the integrated Hamilton population (ICOHP) values. Distances and ICOHP values for all nearest-neighbor contacts and the sums of the latter per cell are listed in Table 3 and Supporting Information Table S3: Table 3 lists the distance ranges and average ICOHP value for each bond type, the total of each type per cell, and the percentage for each type, whereas the same data are broken down in Supporting Information Table S3 for individual bond types. In decreasing order, the major population contributions per bond type come from heteroatomic Mn−Au, Y−Au, and homoatomic Au−Au interactions. However, because of the phase's stoichiometry, the different bond types are reapportioned for the entire unit cell, leading to ICOHP totals that are ∼58% Y−Au, ∼24% Mn−Au, and ∼11% Au−Au. The dominance of the polar bonds is common, but further alteration is brought about by the structure itself and the extremes in the Y_3MnAu_5 composition, 33:11:56 at. %, respectively. The structure does not contain a directly linked Mn network; rather these are coupled by "strong" (highly populated) Mn−Au bonds (Table 3). The Mn atoms themselves lie on a 3-fold axis near z = 1/3 and 2/3, but they are displaced therefrom by bonding differences within the $Mn@Au_8$ clusters, as are visible in Figure 1c and expected according to >20% variations among individual Mn−Au ICOHP values for four different bonds and three types of gold atoms (Supporting Information Table S3). It should be pointed out that our description of bonding in the cell has neglected the large fraction of Y−Au bonds, 47% of the total in Y_3MnAu_5. Of course, these play major roles in the selection and stability of this novel structure.

Beyond the substantial magnetic characteristics of Mn, the relative bonding properties of Au and Y are generally consistent with earlier results among other gold intermetallics. The particular features that make many gold systems significantly different and noteworthy appear to derive from substantial relativistic contributions to its bonding, chemically manifested by both increased binding via the more penetrating 6*s* orbitals and the relative elevation of the $5d^{10}$ states into greater mixing with higher energy valence states on gold and other bonded neighbors, just as seen in Table 3. The enhanced bonding with neighboring atoms can be re-expressed qualitatively in terms of gold atoms' enhanced (Mulliken) electronegativity of 5.77 eV, which approaches those of Te (5.49) and Se (5.89 eV).[38] These effects are also evident in the major importance of Y−Au bonding in the present phase, well in excess of the atom proportions. The electronegativity of Au greatly exceeds that of Y, 3.19 eV (which is in the same general region as that of Mn, 3.72 eV), giving the more extreme polar distribution of Y 4d seen in Figure 8d. Some Y 5s, 5p, and 4d states are naturally involved in bonding with Au 5d around −4.0 to −6.5 eV, but the effective oxidation of Y enhances the displacement of some 4d states to higher energies as the more penetrating Y 5s, 5p become relatively more tightly bound. Very similar 5d distributions were recently found for $R_7Au_2Te_2$ and R_6AuTe_2 (R = Er, Lu) phases in which sheets built from condensed chains of Au-centered trigonal prisms of R are separated by Te monoanions.[36,37] Strong R−Au and R−Te interactions (large

dx.doi.org/10.1021/ja3110208 | J. Am. Chem. Soc. 2013, 135, 910−917

populations) are dominant in both, and the displacements of these 6d orbitals on R to well above E_F are very similar to that calculated here, Figure 8d. The involvements of the Mn 4s and 4p states in Mn−Au bonding in the present phase are rather negligible, in contrast to the appreciable displacements of its 3d states by spin−spin interactions. These do lead to a noticeable bonding contribution of Au 5d to the lower lying Mn 3d spin band as well as a parallel but smaller one from Y 4d (Figure 8b−d).

CONCLUSIONS

In these studies we have discovered and explored the novel rhombohedral intermetallic compound Y_3MnAu_5, which is made up of intergrown and condensed $(Mn@Au_8)_2$ and $Au@Y_6$ polyhedra. The major bonding contributions come from heteroatomic Y−Au and Mn−Au plus smaller and less frequent homoatomic Au−Au interactions. Magnetic studies suggest a planar helical antiferromagnetic ordering of $S = 5/2$ Mn spins in two transitions near 75 and 65 K via strong RKKY-type interactions of Au conduction electrons between high spin $S = 5/2$ Mn atoms. The diversities of Mn 3d, Y 4d, and Au 5d orbital participations in the polar bonding reflect the novelty of the structure.

ASSOCIATED CONTENT

Supporting Information

Tables showing lattice dimensions of R_3MnAu_5 phases, anisotropic displacement parameters for Y_3MnAu_5, and individual interatomic distances and ICOHP values per bond-mol and per cell, figures showing observed and simulated powder X-ray diffraction patterns for Y_3MnAu_5, the Au neighbors about an $Au1@Y_6$ cluster, in-depth view of three layers along $(0\bar{1}1)$, polyhedra about the individual atoms, space lattice of Mn atoms, with dimensions, the antiferromagnetic helical screw model proposed for Y_3MnAu_5, antiferromagnetic T_N versus H, and electrical resistivity and magnetoresistance of Y_3MnAu_5 as a function of T, and a crystallographic information file. This information is available free of charge via the Internet at http://pubs.acs.org.

AUTHOR INFORMATION

Corresponding Author

E-mail: jcorbett@iastate.edu

Notes

The authors declare no competing financial interest.

ACKNOWLEDGMENTS

We acknowledge the valuable advice of G. J. Miller regarding several aspects of the calculations and the bonding. This research was supported by the U.S. Department of Energy (U.S. DOE), Office of the Basic Energy Sciences, Materials Sciences Division. Ames Laboratory is operated for the USDOE by Iowa State University under contract No. DE-AC02-07CH11358.

REFERENCES

(1) Corbett, J. D. *Inorg. Chem.* **2010**, *49*, 13.
(2) Corbett, J. D. In *Chemistry, Structure and Bonding of Zintl Phases and Ions*; Kauzlarich, S., Ed.; VCH Publishers: New York, 1996; Chapter 3.
(3) Pyykkö, P. *Chem. Rev.* **1988**, *88*, 563.
(4) Liu, S. F.; Corbett, J. D. *Inorg. Chem.* **2004**, *43*, 2471.
(5) Liu, S. F.; Corbett, J. D. *Inorg. Chem.* **2004**, *43*, 4988.
(6) Li, B.; Corbett, J. D. *J. Am. Chem. Soc.* **2006**, *128*, 12392.
(7) Lin, Q.; Corbett, J. D. *Inorg. Chem.* **2007**, *46*, 8722.
(8) Dai, J.-C; Corbett, J. D. *Inorg. Chem.* **2007**, *46*, 4592.
(9) Zachwieja, U. *Z. Anorg. Allg. Chem.* **1995**, *621*, 1677.
(10) Zachwieja, U. *J. Alloys Compd.* **1996**, *235*, 7.
(11) Li, B.; Corbett, J. D. *Inorg. Chem.* **2005**, *44*, 6515.
(12) Smetana, V.; Corbett, J. D.; Miller, G. J. *Inorg. Chem.* **2012**, *51*, 1695.
(13) Smetana, V.; Miller, G. J.; Corbett, J. D. *Inorg. Chem.* **2012**, *51*, 7711.
(14) Samal, S. L.; Corbett, J. D. *Inorg. Chem.* **2011**, *50*, 7033.
(15) Samal, S. L.; Lin, Q.; Corbett, J. D. *Inorg. Chem.* **2012**, *51*, 9395.
(16) Gupta, S.; Corbett, J. D. *Inorg. Chem.* **2012**, *51*, 2247.
(17) Rayaprol, S.; Pöttgen, R. *Phys. Rev. B* **2006**, *73*, 214403.
(18) Schappacher, F. M.; Hermes, W.; Pöttgen, R. *J. Solid State Chem.* **2009**, *182*, 265.
(19) Tappe, F.; Schwickert, C.; Pöttgen, R. *Intermetallics* **2012**, *24*, 33.
(20) Shiga, M. *Physica B* **1988**, *149*, 293.
(21) Yamaoka, H.; Tsujii, N.; Jarrige, I.; Takahashi, Y.; Chaboy, J.; Oohashi, H.; Handa, K.; Ide, J.; Tochio, T.; Ito, Y.; Uruga, T.; Yoshikawa, H. *Phys. Rev. B* **2009**, *80*, 115110.
(22) Piqué, C.; Abad, E.; Blanco, J. A.; Burriel, R.; Fernández-Díaz, M. T. *Phys. Rev. B* **2005**, *71*, 174422.
(23) Hardman-Rhyne, K.; Rhyne, J. J.; Prince, E. *Phys. Rev. B* **1984**, *29*, 416.
(24) Dubenko, I. S.; Gaidukova, I. Yu.; Granovsky, S. A.; Gratz, E.; Gurjazkas, D.; Markosyan, A. S.; Müller, H. *Solid State Commun.* **1997**, *103*, 495.
(25) Herzman, N.; Gupta, S.; Corbett, J. D. *Z. Anorg. Allg. Chem.* **2009**, *635*, 848.
(26) Larson, A. C.; Von Dreele, R. B. *GSAS—General Structure Analysis System*; Los Alamos National Laboratory: Los Alamos, NM, 1994.
(27) *SMART*; Bruker AXS, Inc.; Madison, WI, 1996.
(28) Blessing, R. H. *Acta Crystallogr.* **1995**, *A51*, 33.
(29) *SHELXTL*; BrukerAXS, Inc.: Madison, WI, 2000.
(30) Krier, G.; Jepsen, O.; Burkhardt, A.; Andersen, O. K. *TB-LMTO-ASA Program*, version 4.7; Max-Planck-Institut für Festkörperforschung: Stuttgart, Germany, 1995.
(31) Jepsen, O.; Andersen, O. K. *Z. Phys. B* **1995**, *97*, 35.
(32) Dronskowski, R.; Blöchl, P. E. *J. Phys. Chem.* **1993**, *97*, 8617.
(33) Morrish, A. H. *The Physical Principles of Magnetism*; IEEE Press: Piscataway, NJ, 2001.
(34) Johnston, D. C. *Phys. Rev. Lett.* **2012**, *109*, 077201.
(35) Kittel, C. *Introduction to Solid State Physics*, 6th ed.; John Wiley & Sons: New York, 1986.
(36) Chai, P.; Corbett, J. D. *Inorg. Chem.* **2012**, *51*, 3548.
(37) Gupta, S.; Corbett, J. D. *Dalton Trans.* **2010**, *39*, 6074.
(38) Pearson, R. G. *Inorg. Chem.* **1988**, *27*, 734.